Article

Mass Balance Reconstruction for Laohugou Glacier No. 12 from 1980 to 2020, Western Qilian Mountains, China

Jiake Wu [1], Weijun Sun [1,*], Baojuan Huai [1], Minghu Ding [2], Lei Wang [1], Yuzhe Wang [1], Junlong Zhang [1], Wentao Du [3], Jizu Chen [3] and Xiang Qin [3]

1   College of Geography and Environment, Shandong Normal University, Jinan 250014, China
2   Institute of Global Change and Polar Research, Chinese Academy of Meteorological Sciences, Beijing 100081, China
3   Qilian Shan Station of Glaciology and Eco-Environment, State Key Laboratory of Cryospheric Science, Northwest Institute of Eco-Environment and Resources, Chinese Academy of Sciences, Lanzhou 730000, China
*   Correspondence: sunweijun@sdnu.edu.cn

Abstract: A long-series mass balance (MB) of glaciers can be used to study glacier–climate relationships. Using a distributed simplified energy balance model (SEBM) and an enhanced temperature-index model (ETIM), the MB of Laohugou Glacier No. 12 (LHG12) was reconstructed from 1980 to 2020, driven by a calibrated ERA5 reanalysis dataset. The simulation of SEBM performs better than that of ETIM. The results showed that the annual MB of LGH12 is a fluctuating trend of declining from 1980 to 2020, with annual means of -0.39 ± 0.28 m w.e. a^{-1} and cumulative value of -16 ± 4 m w.e. During 1980–1990, the annual MB fluctuated in a small range, while after 1990, LHG12 accelerated melting owing to rising air temperature, with annual means of -0.48 m w.e. a^{-1}, three times as large as that of 1980–1990. The largest mass loss occurred during 2001–2010 at an average rate of -0.57 m w.e. a^{-1}. The average equilibrium line altitude (ELA) was 4976 m a.s.l., and since 1980, the ELA has been increasing at a rate of 37.5 m/10 a. LHG12 is most sensitive to air temperature, and the MB sensitivity reaches -0.51 m w.e. a^{-1} with air temperature increase of 1 °C. The sensitivity of MB to incoming shortwave radiation (+10%) simulated by SEBM is -0.30 m w.e. a^{-1}, three times larger than that simulated by ETIM. This is mainly because the two models have different conditions for controlling melting. Melting is controlled only by air temperature for ETIM, while for SEBM, it is controlled by air temperature and incoming shortwave radiation.

Keywords: mass balance reconstruction; Laohugou Glacier No. 12; glacier models; climate change

1. Introduction

Global mountain glaciers are generally retreating owing to atmospheric warming [1,2]. Mountain glaciers are highly vulnerable to the climate [3–5], and their accelerated melting on the Tibetan Plateau has caused sea level rise [6] and increased the frequency of natural disasters [7]. Maritime glaciers in the Himalayas and southeastern Tibetan Plateau have shrunk significantly [8,9], and mass loss of mountain glacier in the Tianshan Mountains has intensified since the 1970s [10,11]. The Qilian Mountains (QM) are a main glaciation area in China with an arid climate, whose glacier meltwater is crucial for local natural environment [12], but a half-century of glacier melting on the QM has intensified [13,14]. Glacier mass balance (MB) is an important index to measure glacier change [15]. In alpine regions, long-term MB observations are scarce. In recent years, in situ measurements, glacier melting models [15–17], and remote sensing images [18–20] have been widely used to study glacier changes. However, in situ measurements are subject to severe weather, while remote-sensing images are time period-limited.

Glacier melting models are an important way to study glacier MB. The energy–mass balance model has been widely applied to glacier research worldwide [21–23] because

of its good physical basis and excellent performance in single point simulation. Zhang et al. used the energy balance model to reconstruct the glacier MB of glaciers in Hailuogou catchment from 1952 to 2009, and the results showed that the MB loss has been severe in the last 20 years, mainly due to the increase in summer temperatures [9]. The energy balance model is computationally cumbersome when applied to the watershed scale. To reduce the input parameters, Oerlemans [4] proposed a simplified energy balance model (SEBM), all the energy terms except shortwave radiation are simplified as functions related to temperature in the energy balance model. Li's study on Urumqi Glacier No. 1 found that the model had strong spatial transference [24], and MacDougall et al. found that the parameters were mainly sensitive to snow albedo [25]. Linsbauer used SEBM to predict likely changes in Swiss Alps glaciers by the end of the 21st century, and the result suggested temperatures would rise by 2 °C in 2021-50 and 4 °C in 2070-99, leading to an area loss of 60–80% by 2100 [26]. The traditional degree-day model is widely used for long-term glacier MB reconstruction because of its simple structure and few parameters [8,27,28]. Zhang et al. reconstructed the MB of Shiyi glacier using the degree-day model from 1963 to 2016, and the results showed that the MB loss of Shiyi glacier intensified after 1990, which was mainly caused by the cumulative positive temperature increase [15]. Researchers have tried to add shortwave radiation into the degree-day model to improve its physical basis [29,30]. An enhanced temperature-index model (ETIM) [31] was proposed, and temperature affects it very strongly [32]. Gabbi et al. compared the long-term simulation performance of five glacier melting models, and ETIM was the best [33]. Wang et al. used ETIM and discussed the glacier MB and runoff variation in the Beida River Catchment, the continued mass loss of the glaciers caused the equilibrium line attitude (ELA) to rise by 242 m, and the contribution of glacial meltwater to runoff has increased by 6.5% since 2000 [16].

Long-term high spatial and temporal resolution glacier MB reconstruction data, which can help us understand the glacier-atmosphere interaction, are still scarce in the QM [15]. Therefore, we need a suitable model to reconstruct the glacier MB over long time series. The energy balance model and degree-day model have their own advantages and disadvantages in studying glacier MB. At present, the reconstruction of the long-term glaciers MB is still dominated by the degree-day model. In this study, we plan to use SEBM and ETIM to study glacier MB. These two models integrate the advantages of the energy balance model and degree-day model, with few input parameters and a good physical basis [4,30].

The meltwater of Laohugou Glacier No. 12 (LHG12) in the QM is a major water supply (reaching 40%) for Changma River [34], which has a significant influence on the natural environment, production and residents' lives. Glacier MB changes affect the dynamic changes of glacier and its meltwater runoff, thus accurate reconstruction of mountain glacier long-series MB is essential for predicting future runoff changes. The MB of LHG12 has been reconstructed [17,35] using different temperature-index models with a rough resolution. Therefore, we used distributed SEBM and ETIM coupled with shortwave radiation and albedo parameterization schemes to reconstruct glacier MB with higher temporal (1 d) and spatial resolutions (30 m), and the driving data are the calibrated ERA5. The primary purpose of this study is to reconstruct the MB of LHG12 from 1980 to 2020, and we analyzed the impact of climate change on MB and compared the differences between SEBM and ETIM.

2. Study Area and Data

2.1. Study Area

LHG12 (39°26.4′N, 96° 32.5′E, in Figure 1) is the largest valley glacier in the QM in the northeastern part of the Tibetan Plateau. It is about 9.8 km long and has an area of about 20.4 km^2 and an elevation of 4260 to 5400 m [36]. The meltwater of LHG12 in the western QM is a crucial supply source to the Shule River, an inland water system in Gansu Province. In the summer, the average temperature is above 0 °C [37] and precipitation is concentrated. This region is therefore characterized by high altitude, low temperature and low precipitation, which is a typical environment for continental glacier development.
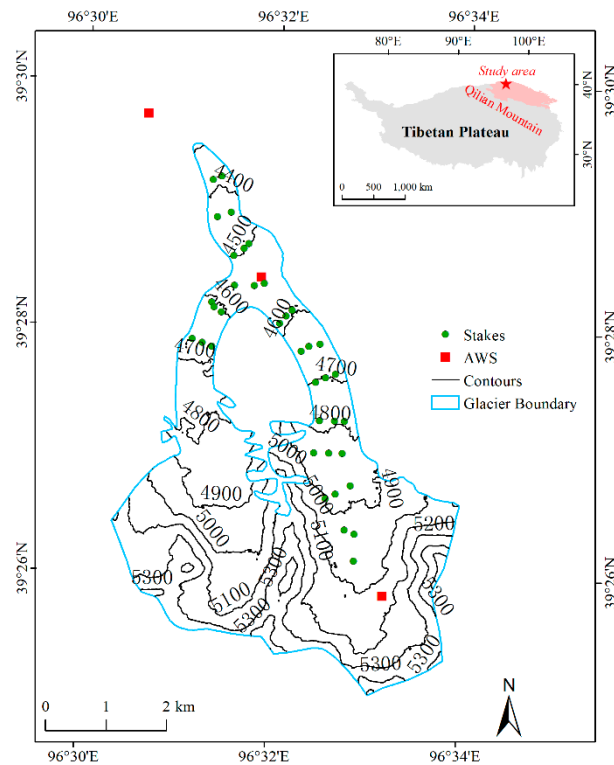
Figure 1. The extent of Laohugou Glacier No. 12 (LHG12) and the location of AWS and stakes, the embedded rectangle displays the positions of LHG12 (red star) and Qilian Mountain Range (pink area) on the Tibetan Plateau.

2.2. Data

The measured meteorological elements were from three automatic weather stations (AWSs) at altitudes of 4200 m a.s.l. (2010–2013), 4550 m a.s.l. (2010–2015) and 5040 m a.s.l. (2010–2013), and they were located at the base camp, ablation area and accumulation area, respectively. Air temperature and incoming and outgoing shortwave radiation were measured. Precipitation was measured by an auto-weighting gauge (T-200B, Geonor). More information about AWS parameters can be found in Sun et al. [38]. The observed data at 4550 m a.s.l. AWS were partially missing from 31 August to 4 September 2015, and the missing values were reconstructed by linear interpolation. The original time step of the data is half an hour, according to which we obtain the daily meteorological elements. The glacier MB data were obtained by stake measurements [35,39]. These data were used for parameter calibration and model validation.

Reconstruction of glacier MB requires long-term and continuous meteorological data, which are difficult to meet with the observed data, so we selected a reanalysis dataset. Huai and others [40] evaluated four reanalysis datasets for the Qilian Mountains and found that the correlation coefficients of most variables of ERA5 were better than others. Wang and others [41] evaluated six reanalysis radiation datasets and found that ERA5 performed best on different time scales in LHG12. Therefore, ERA5 daily temperature, precipitation, and incoming shortwave radiation are the driving data in this study. Bilinear interpolation was used to interpolate the ERA5. Because 4550 m AWS is located on the glacier surface and the collected data have the best temporal continuity, we used the measured data from this AWS (temperature, T_{AWS}; precipitation, P_{AWS}; and incoming shortwave radiation, S_{AWS}) to calibrate ERA5 data (T_{ERA5}, P_{ERA5} and S_{ERA5}) using a linear regression method to eliminate the bias of ERA5 data caused by the coarse resolution and interpolation.

The linear regression equations established between the 4550 m AWS and ERA5 data are as follows:

$$T_{AWS} = 0.7596 \times T_{ERA5} - 4.255 \left(p < 0.001, r = 0.9808, RMSE = 1.6\,^{\circ}\text{C} \right) \tag{1}$$

$$P_{AWS} = 0.6733 \times P_{ERA5} + 0.06823 \left(p < 0.001, r = 0.7207, RMSE = 1.7 \text{ mm w.e} \right) \tag{2}$$

$$S_{AWS} = 0.9727 \times S_{ERA5} - 11.06 \left(p < 0.001, r = 0.8890, RMSE = 40 \text{ W m}^{-2} \right) \tag{3}$$

where T_{ERA5}, P_{ERA5} and S_{ERA5} are the air temperature, total precipitation and incoming shortwave radiation generated by ERA5 interpolation, respectively. Air temperature and precipitation at different altitudes can be calculated according to the temperature lapse rate (TLR) and precipitation gradient (PG). TLR and PG were calculated from the daily temperatures and precipitation measured by AWS at different altitudes from 2010–2013. Figure 2 shows the values of TLR and PG in different months. TLR increases and then decreases over a year with an average of -0.61 °C/100 m. It is relatively high in the summer (June to September) with an average of -0.47 °C/100 m, the maximum value was -0.41 °C/100 m in July, and it is low in winter. PG is lower in the summer and higher in the winter, with an average of 9%/100 m, mainly due to the greater relative variation of precipitation in winter at different altitudes. The results of TLR and PG were consistent with the existing results [42,43]. The initial snow depth comes from solid precipitation that was separated during the previous winter and is assumed to increase with elevation [44]. We set the initial altitude gradient of the snow depth to 0.0008 m/m calculated from the snow depth measured by the stakes.
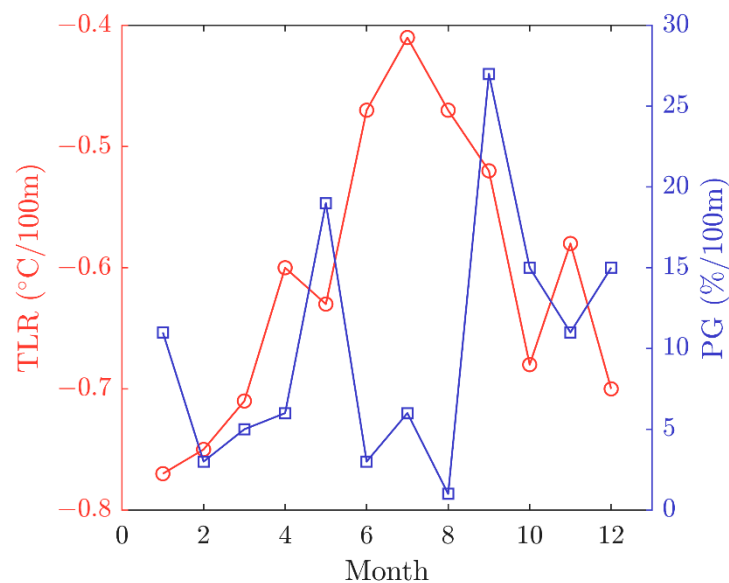
Figure 2. Temperature lapse rates (TLR, °C/100m) and precipitation gradients (PG, %/100 m) in different months.

The digital elevation model (DEM) was ASTER GDEM V3, and its spatial resolution is 30 m. These data were downloaded from the Geospatial Data Cloud (http://www.gscloud.cn/sources/ (accessed on 6 September 2021)). Subsequent MB simulations will be performed on DEM. The slope and aspect of LHG12 will be calculated from the elevation value and used to calculate the incoming shortwave radiation.

3. Methods

3.1. Model Description

The glacier surface MB consists of melt and accumulation, and the equation is given by:

$$MB = P_s - M \tag{4}$$

where MB is the glacier surface MB, P_s is the solid precipitation and M is the glacier melt.

The temperature threshold method is used to distinguish solid precipitation from liquid precipitation [45]. Solid precipitation is calculated as

$$P_s = \begin{cases} P & T < T_s \\ \frac{T_l - T}{T_l - T_s} P & T_s \leq T \leq T_l \\ 0 & T > T_l \end{cases} \tag{5}$$

where P is the total precipitation, and T_l and T_s are the threshold temperatures used to distinguish precipitation types. Here, T_l and T_s are set to $2\,°C$ and $-2\,°C$, respectively [38].

3.1.1. Simplified Energy Balance Model

The simplified energy balance model (SEBM) was proposed by Oerlemans [4]. Compared with the full-component energy balance model, the shortwave radiation part remains unchanged, and the longwave radiation, turbulent flux and conduction heat flux are simplified in the SEBM. The melt energy (Q_m) and glacier melting (M) are calculated by:

$$Q_m = (1 - \alpha) \times S \downarrow + C_0 + C_1 \times T_a \tag{6}$$

$$M = \frac{Q_m}{\rho L_f} \Delta t \tag{7}$$

where α is the albedo, $S \downarrow$ is the incoming shortwave radiation, C_0 (W/m^2) and C_1 ($W/m^2\,°C^{-1}$) are empirical parameters of the temperature-dependent part, T_a ($°C$) is the air temperature, ρ is the density of water ($1000\ kg/m^3$), L_f is the latent heat of fusion ($334{,}000\ J/kg$) and Δt is the time step.

3.1.2. Enhanced Temperature-Index Model

Pellicciotti and others [31] developed a new enhanced temperature-index model (ETIM). This model separates the incoming shortwave radiation from the temperature-dependent energy sources and uses the temperature threshold to determine the occurrence of melting. The melt is calculated as follows:

$$M = \begin{cases} [TF \times T_a + SRF(1 - \alpha)S \downarrow]\Delta t & T_a > 0 \\ 0 & T_a \leq 0 \end{cases} \tag{8}$$

where SRF ($mm\ d^{-1}\ W^{-1}\ m^2$) is the shortwave radiation coefficient and TF ($mm\ d^{-1}\ °C^{-1}$) is the temperature coefficient.

3.1.3. Parameterization

A major index in studying glacier MB is solar radiation [4,46]. Incoming shortwave radiation at different altitudes is calculated as follows [42,47]:

$$S \downarrow = S_{flat} \times \cos \theta \tag{9}$$

$$\cos \theta = \frac{\cos \beta \cos \gamma + \sin \beta \sin \gamma \cos \left(\varphi_{sun} - \varphi_{slope} \right)}{\cos Z} \tag{10}$$

The 4550 m AWS of LHG12 was set up on the relatively flat and open topography, so we assumed that the incoming shortwave radiation observed here reaches the flat ground

(S_{flat}). β is the surface slope, γ and φ_{sun} are the solar zenith and azimuth angles respectively, and φ_{slope} is the aspect.

Many factors have an effect on surface albedo, e.g., cloud cover, surface snow and ice state and solar altitude angle [48,49]. The surface albedo parameterization scheme is very important for the simulation accuracy of the glacier ablation model. Although many albedo parameterization schemes have been proposed, the extension of albedo in different elevation bands and the similarity of glaciers are considered [42]. The parameterization scheme proposed by Jiang et al. [50] for Qiyi Glacier was adopted in this study. Both Qiyi Glacier and LHG12 are located in the Qilian Mountains and are classified as continental glaciers. The albedo for snow and ice is calculated by:

$$\alpha_{snow} = a_1 T_a + a_2 e^{(a_3 \sqrt{n_d})} + a_4 \frac{S \downarrow}{I_{TOA}} \tag{11}$$

$$\alpha_{ice} = b_0 + b_1 T_a \tag{12}$$

$$\alpha = \left(1 - e^{-\frac{d}{d^*}}\right)\alpha_{snow} + e^{-\frac{d}{d^*}}\alpha_{ice} \tag{13}$$

where a_1–a_4, b_0 and b_1 are empirical factors, I_{TOA} is the solar irradiance at top of the atmosphere and n_d is the number of days since the last snowfall. All empirical factors in the formulas are calibrated using the measured data of LHG12.

3.2. Parameter Calibration and Model Uncertainty

The Nash–Sutcliffe efficiency coefficient (R^2), root mean square error $(RMSE)$ and bias $(BIAS)$ are used in the model parameter calibration:

$$R^2 = 1 - \frac{\sum_{i=1}^{n}(O - M)^2}{\sum_{i=1}^{n}\left(M - \overline{M}\right)^2} \tag{14}$$

$$RMSE = \sqrt{\frac{\sum_{i=1}^{n}(O - M)^2}{n}} \tag{15}$$

$$BIAS = \frac{\sum_{i=1}^{n}(M - O)}{n} \tag{16}$$

where O is simulated, M is measured and the bar is the average. R^2 ranges from $-\infty$ to 1. The larger R^2 is, the more reliable the model is.

The empirical parameters of the SEBM (C_0, C_1) and ETIM (TF, SRF) need to be calibrated. Measured MB data in the ablation season were used for parameter calibration. The coefficients were combined in every possible way. The optimal solution corresponds to the maximum R^2. The details on the calibration method can be found in Hock [30] and Pellicciott et al. [31]. According to the calculation results, we obtained the optimal parameter combination for SEBM, which is $C_0 = -68$, $C_1 = 9$ $(R^2 = 0.90)$ and for ETIM is $TF = 3.6$, $SRF = 0.176$ $(R^2 = 0.93)$. For albedo parameters, we used the observed data from 2010 to 2015 for calibration following the method of Jiang et al. [50]. All calibration parameters are presented in Table 1.

Table 1. Parameters of the SEBM and ETIM and the range of parameter change is used to estimate model uncertainty.

Parameters		Unit	Value Used in Model	Change for Model Uncertainty
Albedo	a_1	-	−0.0266	±25%
	a_2	-	0.6785	±25%
	a_3	-	−0.0942	±25%
	a_4	-	−0.1371	±25%
	b_1	-	0.3594	±25%
	b_2	-	−0.0316	±25%
	d	mm	5	±25%
Precipitation separation	T_l	°C	2	1.5~2.5
	T_s	°C	−2	−2.5~−1.5
SEBM	C_1	$W\,m^{-2}\,°C^{-1}$	9	8~10
	C_0	$W\,m^{-2}$	−68	−70~−65
ETIM	TF	$mm\,d^{-1}\,°C^{-1}$	3.6	3.2~4
	SRF	$mm\,m^2\,d^{-1}\,W^{-1}$	0.176	0.17~0.18

The main sources of uncertainty come from the model parameters. Parameters with unknown uncertainty are adjusted by ±25% [15,28], and others are adjusted within the empirical range [8]. We reran the model to obtain the new annual MB by keeping other parameters fixed while varying a single parameter. The maximum standard deviation between the original MB and the new MB series is defined as the model uncertainty [27]. The uncertainty of SEBM is 0.28 m w.e. a^{-1}, then the uncertainty of ETIM is 0.34 m w.e. a^{-1}.

In this study, it was assumed that the glacier area is fixed without change. From 1957 to 2015, LHG12 was estimated to shrink by 1.54 km^2 (7.03%), with a minimal shrinkage rate of 0.03 $km^2\,a^{-1}$ (0.12% a^{-1}) [36]. Therefore, we believe that it is reasonable to use a fixed glacier area to simulate MB, and the resulting error can be ignored.

3.3. Model Verification

To verify the simulation accuracy of incoming shortwave radiation, we compared the observed and modeled incoming shortwave radiation from 5040 m AWS in 2010–2013. The 5040 m AWS is located on the glacier surface, and the collected incoming shortwave radiation data have a longer time series and better quality. There is a close agreement between the modeled and observed incoming shortwave radiation (R^2 = 0.9, RMSE = 29 W m^{-2} and BIAS= −16.7 W m^{-2}) in Figure 3, the parameterization slightly underestimates the incoming shortwave radiation. To assess the accuracy of the SEBM and ETIM, we verify the modeled MB using observed MB elevation gradients for each hydrological year between 2009 and 2015 in Figure 4 (data from Chen et al. [35]; note that the MB of 2012/2013 was not included). The simulated value of SEBM was closer to the observed MB, with lower RMSE (mean SEBM RMSE = 0.39 m w.e., mean ETIM RMSE = 0.44 m w.e.) and the absolute BIAS was smaller (mean SEBM RMSE = −0.17 m w.e., mean ETIM RMSE = −0.21 m w.e.). The modeled values can describe MB changes well, among which 2009/10 was the best (RMSE = 0.33 m w.e., SEBM BIAS = −0.06 m w.e., ETIM BIAS = 0.09 m w.e.), while 2010/11 was the worst (SEBM: RMSE = 0.45 m w.e. and BIAS = -0.31 m w.e., ETIM: RMSE = 0.56 m w.e. and BIAS = −0.48 m w.e.). The ablation area showed large differences, with overestimation of MB in 2010/11, 2011/12 and 2014/15, and underestimation in 2013/14.
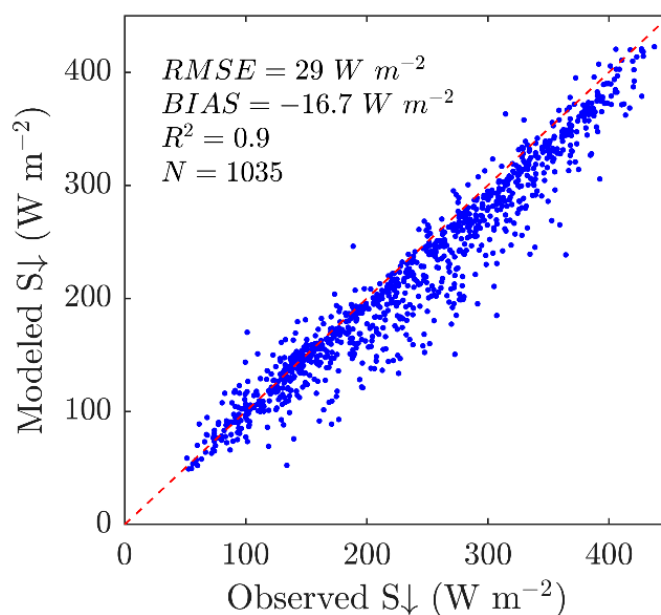
Figure 3. Observed and modeled incoming shortwave radiation (S↓) at 5040 m AWS.
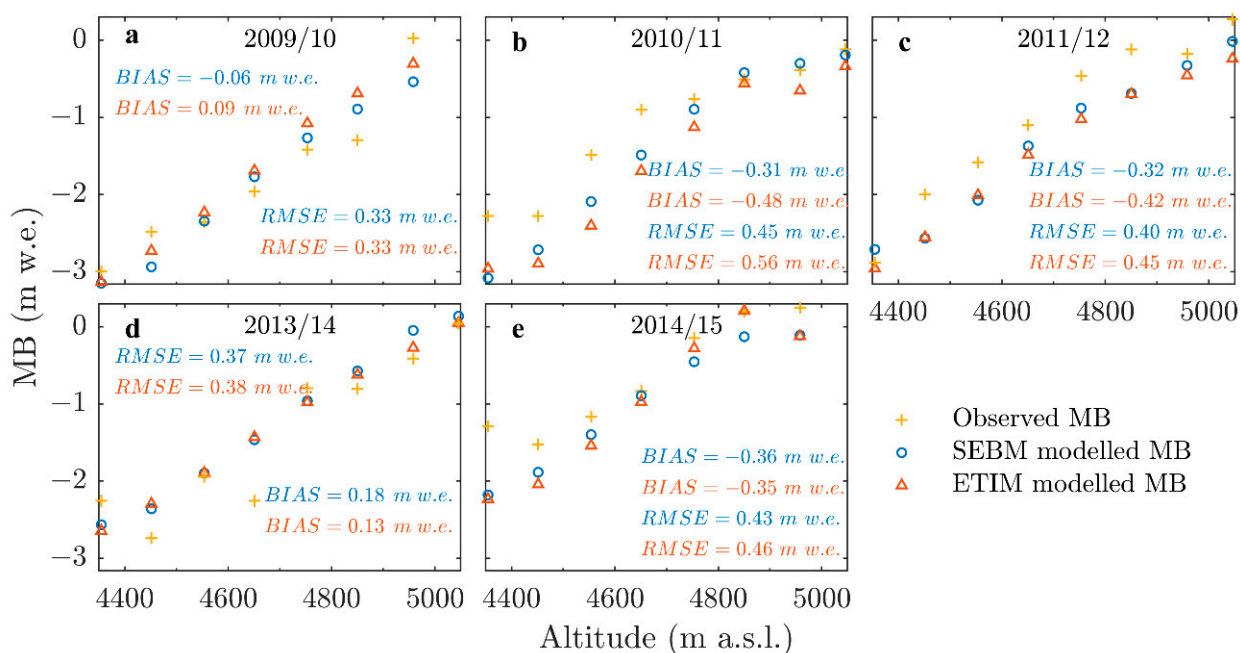
Figure 4. Observed and modeled mass balance (MB) at different altitudes from 2009/10 to 2014/15 (**a–e**, excluding 2012/13). Blue and red symbols represent SEBM and ETIM, respectively.

4. Result

4.1. Meteorological Conditions

The overall meteorological conditions of LHG12 from 1980 to 2020 are shown in Figure 5. Annual, summer and winter temperatures all showed an obvious upward trend (Figure 5a); the warming rates were 0.27 °C/10 a, 0.38 °C/10 a, and 0.21 °C/10 a, respectively, and were similar to 0.33 °C/10 a in the Tibetan Plateau [51]. The fastest warming rates of both annual temperature (0.82 °C/10 a) and winter temperature (0.8 °C/10 a) occured between 2011 and 2020. The fastest summer temperature warming rate was 1.45 °C/10 a from 1991 to 2000. The annual temperature varied between −12.6 (1983) to −10.6 °C (1998), with an average of −11.6 °C. The summer temperature ranged from −3.8 °C in 1984 to −1.05 °C in 2016, with an average of −2.33 °C. The temper-

ature in the summer was higher, with an average of $-2.3\ °C$, and the highest temperature in July was $-0.15\ °C$, as shown in Figure 5b.

Figure 5. Meteorological elements of LHG12 from calibrated ERA5 during 1980 to 2020: (**a**) annual, winter and summer precipitation (Prec) and temperature (T), (**b**) monthly mean temperature and precipitation, and (**c**) annual, summer, winter and monthly mean incoming shortwave radiation (S↓).

LHG12 had a tendency to become wet from 1980 to 2020, and the annual precipitation change rate was 18.9 mm/10 a which are faster than the national average of 11.72 mm/10 a [52]. Summer and winter precipitation change rates were 14.3 mm/10 a and 4.5 mm/10 a, singly. The average annual precipitation was 474 mm w.e., then the average summer precipitation was 288 mm w.e. This area was influenced by the westerly circulation all year round, and the precipitation was mainly concentrated in the summer (Figure 5b). In July, precipitation reached its peak value of 100 mm w.e. in Figure 5b, while precipitation is rare in winter. Figure 5c shows the variation in incoming shortwave radiation during the study period. Annual and summer incoming shortwave radiation showed a decreasing trend, while winter incoming shortwave radiation showed a slight increasing trend. However, the albedo decreased during the study period, indicating that the net shortwave radiation received by the glacier surface actually increased. Incoming shortwave radiation reached its peak ($275\ W\ m^{-2}$) in May and was higher in the summer, its average was $236\ W\ m^{-2}$.

4.2. Annual and Cumulative MB

We reconstructed the annual, cumulative and season MB, equilibrium line altitude (ELA) and accumulation area ratio (AAR) of LHG12 from 1980 to 2020 using SEBM and ETIM. In Figure 6, we can see that the annual MB and cumulative MB simulated by the SEBM and ETIM are very close to each other and change in the same trend. ETIM generally simulates more mass loss than SEBM. The two groups reconstructed annual MB showed good consistency with the measured glacier-wide MB [39] in Figure 6, and SEBM (RMSE = 0.12 m w.e.) performed better than ETIM (RMSE = 0.2 m w.e.). Therefore, we take the simulation results of SEBM as an example for analysis. We will also display the simulation results of ETIM in the parentheses below.
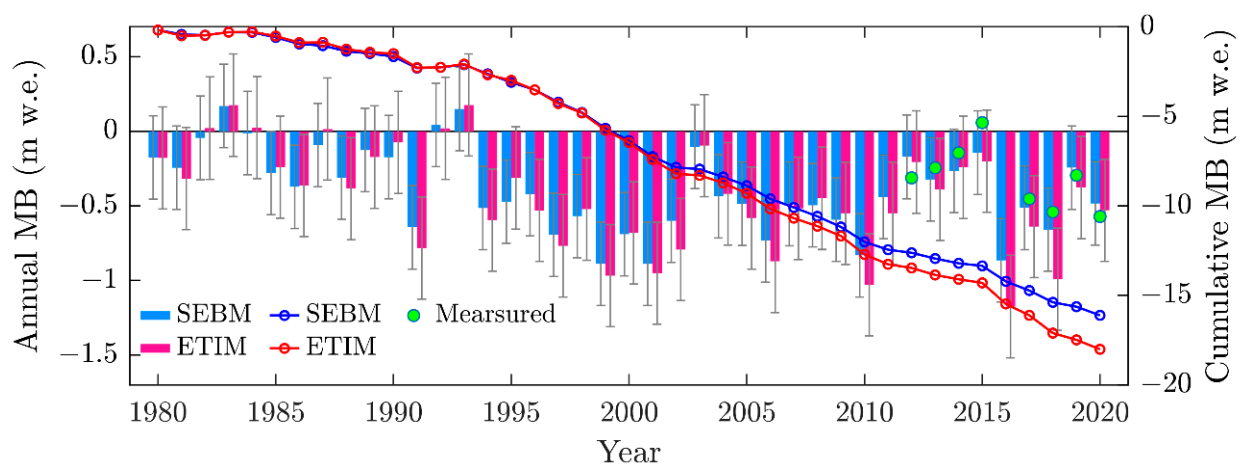
Figure 6. The measured annual MB (green dot), the modeled annual and cumulative MB by SEBM (blue) and ETIM (red).

The simulation result displays that the annual MB of LHG12 is a fluctuating declining trend, and since the 1990s, the mass deficit increased, and the annual MB was mainly negative. The SEBM (ETIM) modeled results showed that the positive maximum annual MB was 0.17 m w.e. (0.18 m w.e.) in 1983 (1993), the mass loss was most severe in 2001 (2016) with an annual MB of −0.89 m w.e. (−1.17 m w.e.), and the average annual MB is −0.39 ± 0.28 m w.e. a^{-1} (−0.44 ± 0.34 m w.e. a^{-1}). In the QM, the average annual MB in the Beida River catchment is −0.158 m w.e. (1975–2013) [16], and the average annual MB of Shiyi Glacier is −0.24 m w.e. (1963–2017) and is −0.6 m w.e. after 1990 [15], which verges on that of LHG12 (−0.5 m w.e.). Although the peaks modeled by the two models occurred in different years, 2001 and 2016 were both years of severe mass deficit, and 1983 and 1993 are years of strong accumulation. SEBM (ETIM) modeled the cumulative MB is −16.1 ± 4 m w.e. (−18 ± 4 m w.e.). During 1989–2015, the cumulative MB of LHG12 from DEM differencing is −14.36 m w.e. [53], which is very approximate to our results (SEBM: −12 m w.e., ETIM: −13.2 m w.e.).

Through the Mann–Kendall test, we found that the abrupt point of the annual MB is in 1990. During 1980–1990, annual MB was relatively stable and fluctuated in a small range, with an average annual MB of −0.15 m w.e. a^{-1}, while during 1991–2020, the annual MB was continuous negative and greatly changed, with an average annual MB of −0.48 m w.e. a^{-1}, the average annual MB after 1990 was more than three times that of in 1980–1990. We divided the study period into four subperiods, period I (1981–1990), period II (1991–2000), period III (2001–2010) and period IV (2011–2020). In the four subperiods, the cumulative MB is −1.48 m w.e., −4.70 m w.e., −5.65 m w.e. and −4.10 m w.e., respectively. Period III has the largest mass loss, almost four times that of period I.

4.3. Seasonal MB

The seasonal MB can better reflect the interaction between glaciers and the atmosphere [8,54]. The seasonal MB reconstructed by SEBM and ETIM is exhibited in Figure 7. We note that the winter MB remains stable, the summer MB shows an obvious downward trend ($p < 0.05$), and the changing trend is consistent with that of the annual MB. ETIM typically simulates more mass loss than SEBM during intense melt summers. The summer MB simulated by SEBM (ETIM) ranged from $-1.08 \sim 0.02$ m w.e. ($-1.37 \sim 0.02$ m w.e.), and its mean was -0.57 m w.e. (-0.62 m w.e.). Winter MB simulated by the two models were similar. The summer MB fluctuates greatly. SEBM (ETIM) simulation results show that during 1980–1990, the summer MB varied from $-0.57 \sim 0.02$ m w.e. ($-0.56 \sim 0.02$), its average is 0.33 m w.e. a^{-1} (-0.32 m w.e. a^{-1}), and the cumulative summer MB is -3.6 m w.e. (-3.5 m w.e.). Then, the summer MB fluctuated from $-1.08 \sim -0.02$ m w.e. ($-1.37 \sim -0.02$ m w.e.), the average was -0.66 m w.e. a^{-1} (-0.74 m w.e. a^{-1}), and cumulative summer MB was -19.9 m w.e. (-22.1 m w.e.) after 1990. The two models simulated a similar summer MB in 1980–1990, and summer melting rate accelerated after 1990, the average summer MB after 1990 was twice as large as in 1980–1990. In the four subperiods, the cumulative summer MB is -3.28 m w.e., -6.38 m w.e., -7.58 m w.e. and -5.93 m w.e., respectively. Period III lost the most mass in the summer, more than twice as much as period I.
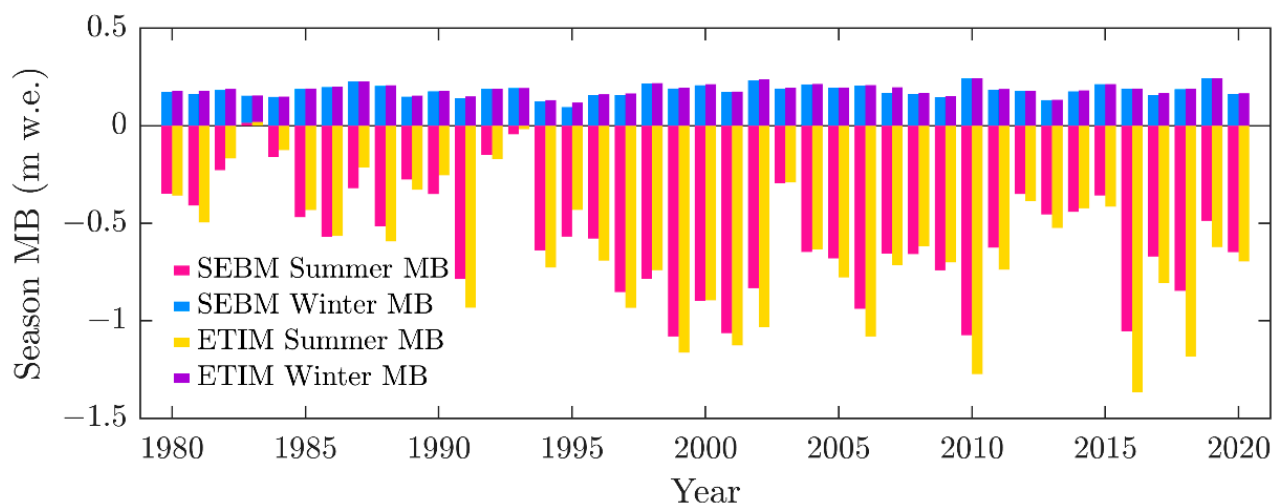
Figure 7. Summer and winter mass balance modeled by SEBM and ETIM.

4.4. ELA and AAR

The ELA was obtained by linear regression of the space MB. Figure 8a shows how the ELA changes during the study period. The ELA modeled by ETIM was higher than that modeled by SEBM, and the ELA had a trend of upward fluctuation. For SEBM (ETIM), the lowest ELA occurred at the smallest loss of MB and was 4697 m a.s.l. (4713 m a.s.l.) in 1983 (1993), and the highest ELA occurred at the most intense loss of MB and was 5175 m a.s.l. (5293 m a.s.l.) in 2001 (2016), and the average ELA was 4976 m a.s.l. (5045 m a.s.l.). Since 1980, the ELA has been increasing at a rate of 37.5 m/10 a (49.8 m/10 a). In the Beida River catchment, which is also located in the Qilian Mountains, ELA increased by 242 m from 1957 to 2013 [16]. From Figure 8c, we can see the excellent correlation between annual MB and ELA. The greater the mass loss is, the higher the ELA (SEBM $R^2 = 0.90$ and ETIM $R^2 = 0.91$, $p < 0.001$). An increase of 0.1 m w.e. in mass loss and a rise of 39 m in ELA.
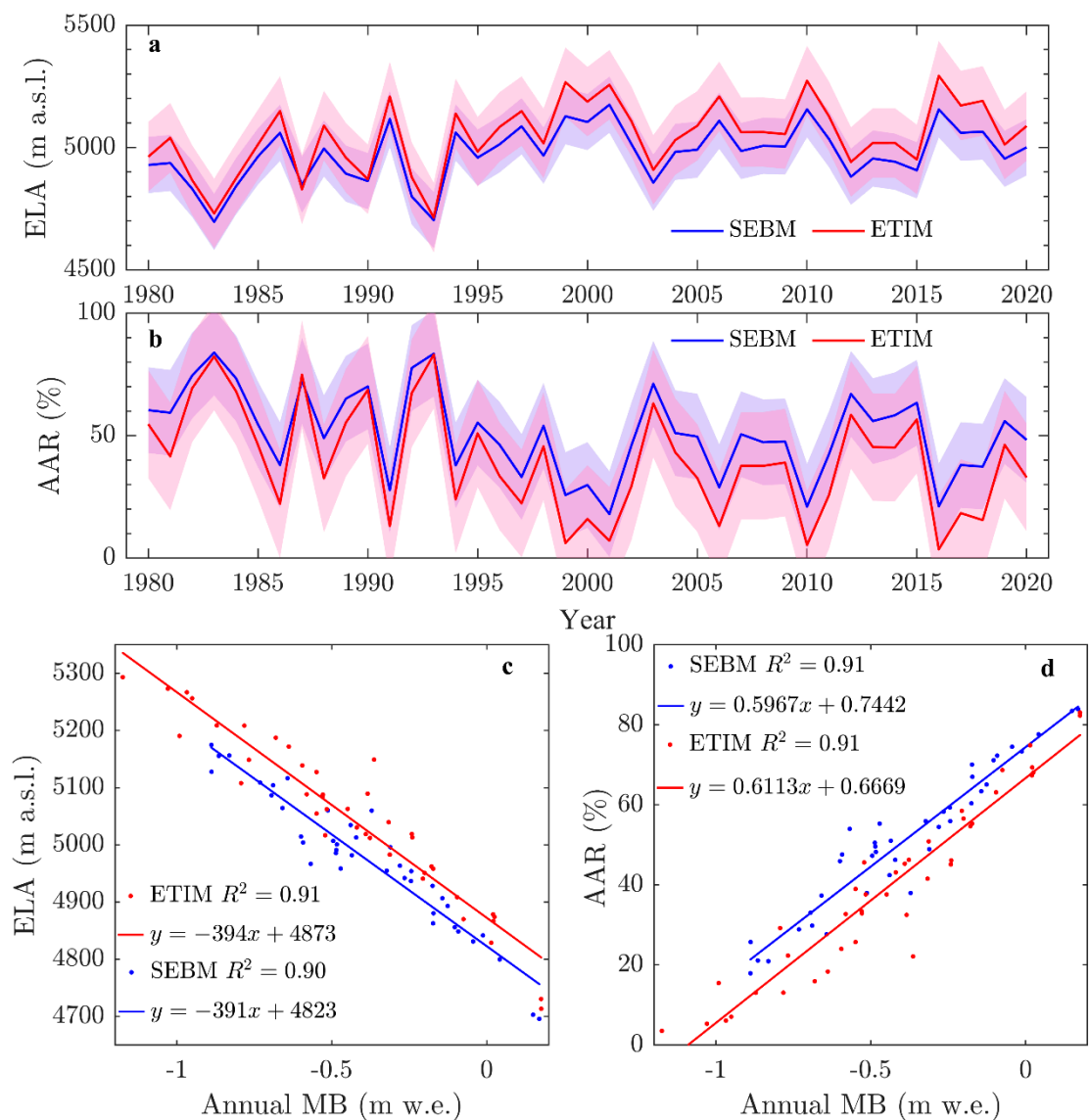
Figure 8. (**a**) Equilibrium-line altitude (ELA) and (**b**) accumulation area ratio (AAR) modeled by SEBM and ETIM, and fitting function of ELA (**c**) and AAR (**d**) with annual MB.

The AAR is obtained using the corresponding annual ELA. In contrast to ELA, AAR has a downward trend in Figure 8b. The simulation results of the SEBM are generally higher than those of the ETIM. For the former, the maximum AAR was 84%, which was similar to the latter (83%), and the minimum AAR was 18%, which is five times that of the latter. A higher AAR corresponds to a positive annual MB with glacier MB accumulation, such as in 1983 and 1993, while the year corresponding to a lower AAR has severe glacier mass loss, such as in 2001 and 2016. From Figure 8d, we can see the excellent correlation between annual MB and AAR. The stronger the mass accumulation is, the larger the AAR (SEBM $R^2 = 0.91$ and ETIM $R^2 = 0.91$, $p < 0.001$). There is an increase in mass loss of 0.1 m w.e. and a decrease in the AAR of approximately 6%. From 1980–2020, the AAR modeled by the SEBM and ETIM shrank by 12% and 22%, respectively. The differences between ELA and AAR are explained in Section 5.2.

5. Discussion

5.1. Response of MB to Climate Change

Changes in mountain glaciers MB represents local climate change. There was good agreement between the annual MB and annual temperature (SEBM: R = −0.64, ETIM: R = −0.64, $p < 0.001$), and the consistency between the summer MB and summer temperature was better (SEBM: R = −0.89, ETIM: R = −0.88, $p < 0.001$). The intensification of glacier mass loss is closely bound up with temperature rise. During the study period, snowfall had a weak upward trend as shown in Figure 9a, but it did not pass the significance test of $p < 0.05$. In general, an increase in snowfall will lead to an increase in albedo and thus reduce melting. However, albedo showed an obvious downward trend in Figure 9b, and the correlation between snowfall and annual MB was not close. The reasons for this will be discussed below; mass losses from warmer temperatures are hard to compensate for by increased snowfall. The decreased albedo may be because the increased summer temperature makes the snow deteriorate faster, the AAR keeps decreasing with the intensification of mass loss (in Figure 8b), and the glacier area covered by snow decreases. Additionally, decreased albedo would lead to increased net shortwave radiation, which would increase the melt and further contribute to decreased albedo.
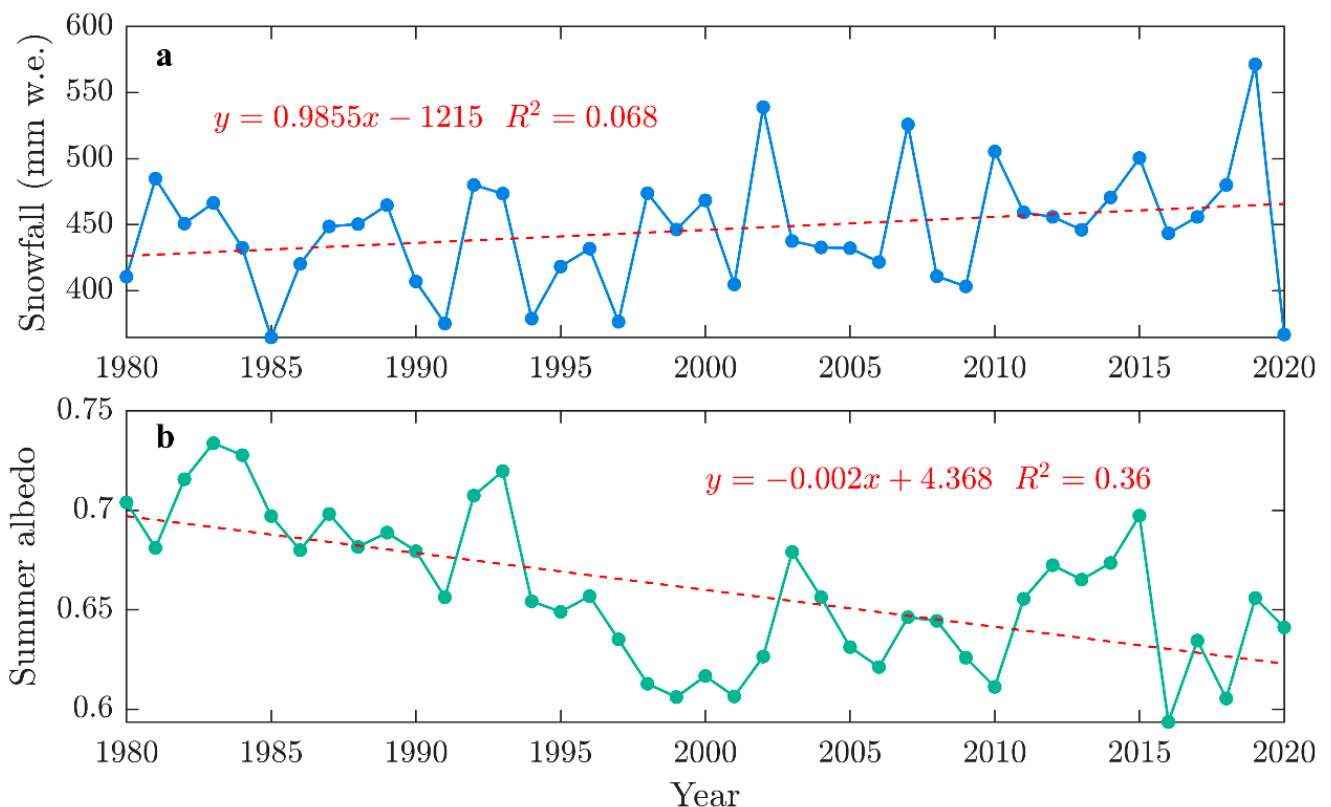
Figure 9. Changes of snowfall (**a**) and summer albedo (**b**) during the study period.

To explore the response of MB to climate change, we set up different scenarios of independent changes in temperature, precipitation and incoming shortwave radiation. Changes in temperature from −2 to +2 °C with a step of 0.5 °C were observed, and the precipitation and incoming shortwave radiation changed from −20% to +20% with a step of 5%. The sensitivity tests of the model parameters are performed by varying one parameter and keeping the others fixed. The sensitivity test results are shown in Figure 10. The MB is more sensitive to the increase in meteorological elements than to the decrease. LHG12 is most sensitive to temperature, followed by incoming shortwave radiation, and finally precipitation. In Figure 10, the MB sensitivity to temperature changes simulated by ETIM was slightly higher than that simulated by SEBM; when the temperature changed by +1 °C,

the MB sensitivity modeled by SEBM (ETIM) was -0.51 m w.e. a^{-1} (-0.61 m w.e. a^{-1}). Our result was similar to that of Qiyi Glacier [16] but lower than that of Shiyi Glacier [15] and Parlung No. 94 Glacier [55].
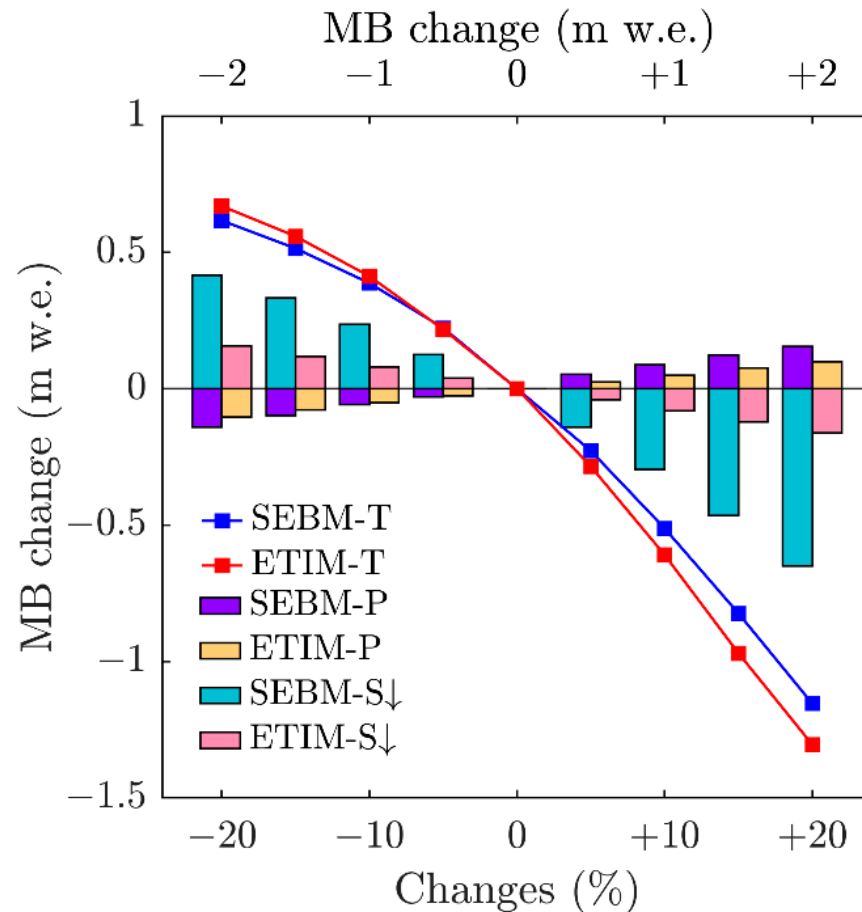
Figure 10. Sensitivities of MB to changes in meteorological elements, including air temperature (T), precipitation (P) and incoming shortwave radiation (S↓).

The MB sensitivity of the two models to incoming shortwave radiation is very different. When the incoming shortwave radiation changed by $+10\%$ (-10%), the MB sensitivity of SEBM was -0.30 m w.e. a^{-1} ($+0.24$ m w.e. a^{-1}), roughly 3~4 times that of ETIM. This is mainly because whether to simulate melting or not, ETIM is controlled only by temperature, but SEBM is controlled by air temperature and shortwave radiation. The MB sensitivity to precipitation for SEBM was greater than that for ETIM. The MB sensitivity to precipitation was minimal; when precipitation changes $\pm10\%$, the MB sensitivity of SEBM (ETIM) was ±0.09 m w.e. a^{-1} (±0.05 m w.e. a^{-1}). The sensitivity of LHG12 to precipitation was similar to that of Qiyi Glacier [56] but lower than that of Shiyi Glacier [15]. From 1980 to 2020, there was a 0.77 °C rise in annual temperature, and a change in annual MB of -300 to -400 mm w.e., but the annual precipitation increased by only 56 mm w.e. By and large, mass loss of glacier due to rising temperatures was difficult to compensate for by increased precipitation. The results were similar to those of Wang in the Qilian Mountains [39].

5.2. Model Differences

Figure 11 shows the multi-year average annual MB of LHG12 simulated by the two models. Glacier surface MB increase positively with elevation. There are some differences between the multi-year simulations. First, we can see in Figure 11 that SEBM simulates more mass loss at lower elevations and the ELA (the dividing line between yellow and blue) of ETIM was higher than that of SEBM. Similarly, ETIM simulated a higher ELA and smaller

AAR in Figure 8a,b. This is mainly because of the different structure of the two models. For SEBM, melting occurred when $Q_m > 0$, and melting occurred when the temperature was >0 °C for ETIM. We used Δ melt (Δ melt = melt_SEB–melt_ETI) to denote the difference in melt between SEBM and ETIM. If Δ melt is >0, it means that SEBM simulates more melting, whereas ETIM simulates more melting. In Figure 12a, we can see that when the temperature is >0 °C, Δ melt is <0 for most combinations of temperature and net shortwave radiation, and Δ melt is >0 only when the temperature is low (<5 °C) and the net shortwave radiation is very high (>200 W m^{-2}). In addition, when the temperature is <0 °C, ETIM no longer simulates melt, and SEBM melt occurs only when net shortwave radiation is high (>100 W m^{-2}). We take the altitude of 4300 m a.s.l. (ablation area) and 5000 m a.s.l. (near ELA) as examples to analyze the reasons for the difference between the simulation results of the two models. In Figure 12b (4300 m a.s.l.), when the temperature is <0 °C, due to the strong net shortwave radiation, SEBM has more days to melt, and the amount of melting is relatively large, so SEBM simulates more melting (Δ melt > 0). As the altitude increases, melting decreases, and increasing snow cover leads to an increase in albedo and a decrease in net shortwave radiation. In Figure 12c (5000 m a.s.l.), when the temperature is less than 0 °C, the number of days and amount of SEBM melting decreased. In addition, since SEBM is very sensitive to shortwave radiation, the melting of SEBM will decrease rapidly compared with ETIM when the temperature is >0 °C due to the decrease of net radiation, so the Δ melt difference will increase negatively. Therefore, ETIM simulates more melt at low temperatures at high altitudes, which results in higher ELA and smaller AAR. In addition, we also found that the spatial distribution of MB in Figure 11a was chaotic, especially in the middle of the glacier. This is mainly due to the different sensitivities of the two models to incoming shortwave radiation. SEBM is more sensitive to incoming shortwave radiation, and regions with higher MB at similar altitudes correspond to regions with lower incoming shortwave radiation.
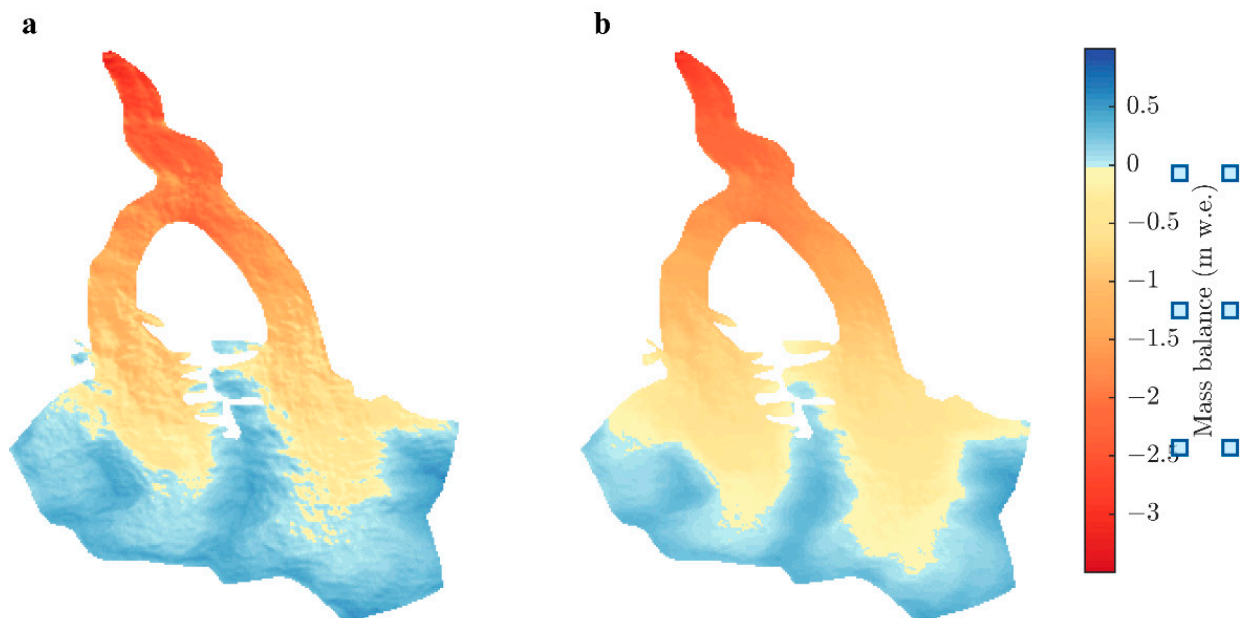
Figure 11. The multi-year average annual MB of LHG12 modeled by SEBM (**a**) and ETIM (**b**).
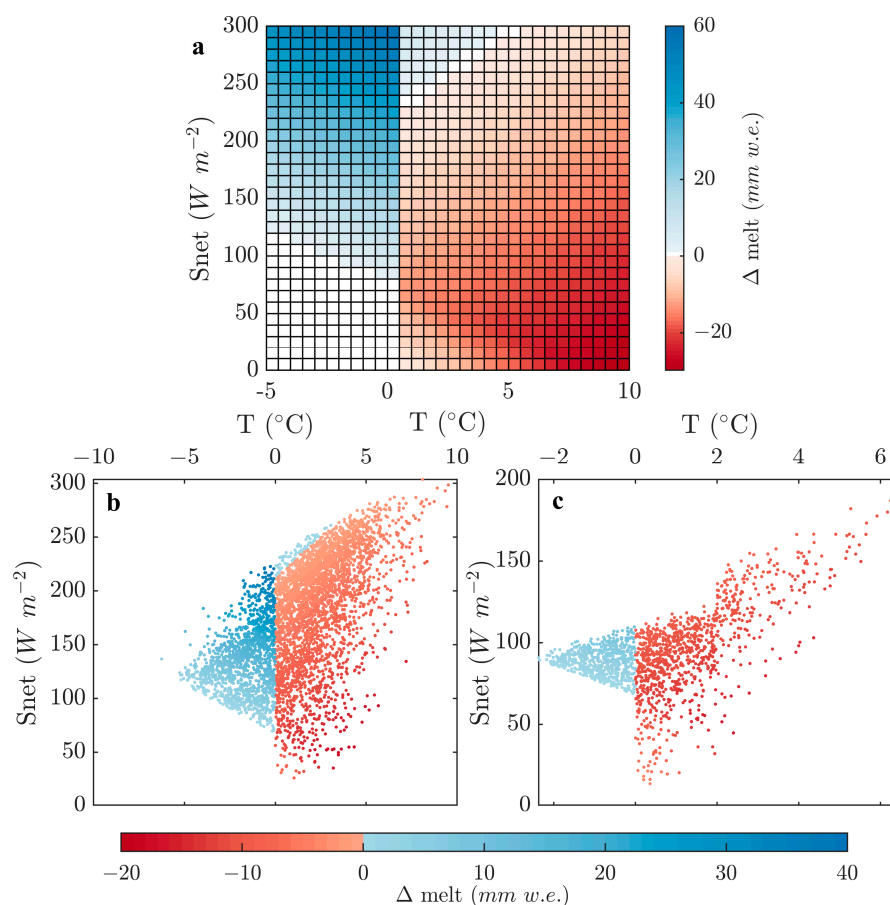
Figure 12. (**a**) Melting difference between SEBM and ETIM at different combinations of temperature and net shortwave radiation, (**b**) melting difference at 4300 m a.s.l., and (**c**) melting difference at 5000 m a.s.l., Δ melt = melt_SEB − melt_ETI, and a positive (negative) value shown in blue (red) means that the SEBM (ETIM) simulates more melting.

6. Conclusions

We used measured meteorological data and in situ MB to calibrate the two empirical models (SEBM and ETIM). Using the calibrated ERA5 as the driving data, annual and seasonal MB of LHG12 from 1980–2020 are reconstructed, and ELA and AAR are also presented. DEM difference results and measured MB were used to verify the model. We also discussed the response of LHG12 to climate change and model differences between SEBM and ETIM.

The simulation performance of SEBM is better than ETIM. The results showed that during study period, LHG12 is mainly in mass deficit, and the melt is intensified after 1990. The annual MB m is -0.39 ± 0.28 m w.e. a^{-1}, and the cumulative MB is -16.1 ± 4 m w.e. After 1990, annual MB was continuous negative and greatly changed, with an average annual MB of -0.48 m w.e. a^{-1} which was more than three times that of in 1980–1990. The winter MB remains stable, and the summer MB mainly determines annual MB, and the change trend is consistent with annual MB. Like the annual MB, THE summer melting rate accelerated after 1990, the average summer MB after 1990 is -0.48 m w.e. a^{-1}, twice that of in 1980–1990. The mean ELA is 4976 m a.s.l. and since 1980, the ELA has been increasing at a rate of 37.5 m/10 a. In addition, an increase of 0.1 m w.e. in mass loss and a rise of 39 m in ELA were modeled.

The intensified mass loss in LHG12 is mainly due to increasing temperature. LHG12 was most sensitive to temperature change, and the MB sensitivity is -0.51 m w.e. a^{-1} $^{\circ}C^{-1}$. SEBM is obviously more sensitive to incoming shortwave radiation than ETIM; when incoming shortwave radiation changes +10%, the MB sensitivity is -0.30 m w.e. a^{-1} for

SEBM, roughly equivalent to four times for ETIM. When precipitation changed by $\pm 10\%$, the MB sensitivity was about $\pm\,0.09$ m w.e. a^{-1}. ETIM simulates a higher ELA and a smaller AAR. There are differences in sensitivity and spatial distribution of MB between SEBM and ETIM, which are mainly because of the different structures of the two models. Melting is controlled by temperature and incoming shortwave radiation, so it can also occur when the temperature is less than 0 °C, but for ETIM, it is controlled only by temperature, so it only occurs when the temperature is larger than 0 °C.

This study accurately simulated the MB long-term trend of a single glacier, which is a crucial step in developing high-precision numerical simulations of MB at the watershed scale. The models and parameterization need to be further enhanced. Additionally, this study also provides new research ideas for glaciers that lack observations in alpine regions.

References

1. Marzeion, B.; Jarosch, A.H.; Gregory, J.M. Feedbacks and mechanisms affecting the global sensitivity of glaciers to climate change. *Cryosphere* **2014**, *8*, 59–71. [CrossRef]
2. Vuille, M.; Carey, M.; Huggel, C.; Buytaert, W.; Rabatel, A.; Jacobsen, D.; Soruco, A.; Villacis, M.; Yarleque, C.; Elison Timm, O.; et al. Rapid decline of snow and ice in the tropical Andes—Impacts, uncertainties and challenges ahead. *Earth Sci. Rev.* **2018**, *176*, 195–213. [CrossRef]
3. Oerlemans, J. Climate sensitivity of glaciers in southern Norway: Application of an energy-balance model to Nigardsbreen, Hellstugubreen and Alfotbreen. *J. Glaciol.* **1992**, *38*, 223–232. [CrossRef]
4. Oerlemans, J. *Glaciers and Climate Change*; CRC Press: Boca Raton, FL, USA, 2001.
5. Deng, H.; Chen, Y.; Li, Y. Glacier and snow variations and their impacts on regional water resources in mountains. *J. Geogr. Sci.* **2019**, *29*, 86–102. [CrossRef]
6. Marzeion, B.; Jarosch, A.; Hofer, M. Past and future sea-level change from the surface mass balance of glaciers. *Cryosphere* **2012**, *6*, 1295–1322. [CrossRef]
7. Yao, T.; Yu, W.; Wu, G.; Xu, B.; Yang, W.; Zhao, H.; Wang, W.; Li, S.; Wang, N.; Li, Z.; et al. Glacier anomalies and relevant disaster risks on the Tibetan Plateau and surroundings. *Chin. Sci. Bull.* **2019**, *64*, 2770–2782.
8. Azam, M.F.; Srivastava, S. Mass balance and runoff modelling of partially debris-covered Dokriani Glacier in monsoon-dominated Himalaya using ERA5 data since 1979. *J. Hydrol.* **2020**, *590*, 125432. [CrossRef]
9. Zhang, Y.; Hirabayashi, Y.; Liu, S. Catchment-scale reconstruction of glacier mass balance using observations and global climate data: Case study of the Hailuogou catchment, south-eastern Tibetan Plateau. *J. Hydrol.* **2012**, *444–445*, 146–160. [CrossRef]
10. Zheng, Z.; Hong, S.; Deng, H.; Li, Z.; Jin, S.; Chen, X.; Gao, L.; Chen, Y.; Liu, M.; Luo, P. Impact of Elevation-Dependent Warming on Runoff Changes in the Headwater Region of Urumqi River Basin. *Remote Sens.* **2022**, *14*, 1780. [CrossRef]
11. Narama, C.; Kääb, A.; Duishonakunov, M.; Abdrakhmatov, K. Spatial variability of recent glacier area changes in the Tien Shan Mountains, Central Asia, using Corona (~1970), Landsat (~2000), and ALOS (~2007) satellite data. *Glob. Planet. Chang.* **2010**, *71*, 42–54. [CrossRef]
12. Guo, Z.; Wang, N.; Shen, B.; Gu, Z.; Wu, Y.; Chen, A. Recent Spatiotemporal Trends in Glacier Snowline Altitude at the End of the Melt Season in the Qilian Mountains, China. *Remote Sens.* **2021**, *13*, 4935. [CrossRef]
13. Yao, T.; Thompson, L.; Yang, W.; Yu, W.; Gao, Y.; Guo, X.; Yang, X.; Duan, K.; Zhao, H.; Xu, B.; et al. Different glacier status with atmospheric circulations in Tibetan Plateau and surroundings. *Nat. Clim. Chang.* **2012**, *2*, 663–667. [CrossRef]

14. Sun, M.; Liu, S.; Yao, X.; Guo, W.; Xu, J. Glacier changes in the Qilian Mountains in the past half-century: Based on the revised First and Second Chinese Glacier Inventory. *J. Geogr.Sci.* **2018**, *28*, 206–220. [CrossRef]

15. Zhang, H.; Li, Z.; Zhou, P. Mass balance reconstruction for Shiyi Glacier in the Qilian Mountains, Northeastern Tibetan Plateau, and its climatic drivers. *Clim. Dyn.* **2020**, *56*, 969–984. [CrossRef]

16. Wang, S.; Yao, T.; Tian, L.; Pu, J. Glacier mass variation and its effect on surface runoff in the Beida River catchment during 1957–2013. *J. Glaciol.* **2017**, *63*, 523–534. [CrossRef]

17. Wang, L.; Qin, X.; Chen, J.; Zhang, D.; Liu, Y.; Li, Y.; Jin, Z. Reconstruction of the glacier mass balance in the Qilian Mountains from 1961 to 2013. *Arid Zone Res.* **2021**, *38*, 1524–1533.

18. Liu, Y.; Qin, D.; Jin, Z.; Li, Y.; Xue, L.; Qin, X. Dynamic Monitoring of Laohugou Glacier No. 12 with a Drone, West Qilian Mountains, West China. *Remote Sens.* **2022**, *14*, 3315. [CrossRef]

19. Pan, B.; Cao, B.; Wang, J.; Zhang, G.; Zhang, C.; Hu, Z.; Huang, B. Glacier variations in response to climate change from 1972 to 2007 in the western Lenglongling mountains, northeastern Tibetan Plateau. *J. Glaciol.* **2012**, *58*, 879–888. [CrossRef]

20. Cao, B.; Guan, W.; Li, K.; Pan, B.; Sun, X. High-resolution monitoring of glacier mass balance and dynamics with unmanned aerial vehicles on the Ningchan No. 1 Glacier in the Qilian Mountains, China. *Remote Sens.* **2021**, *13*, 2735. [CrossRef]

21. Ding, M.; Yang, D.; Broeke, M.R.; Allison, I.; Xiao, C.; Qin, D.; Huai, B. The Surface Energy Balance at Panda 1 Station, Princess Elizabeth Land: A Typical Katabatic Wind Region in East Antarctica. *J. Geophys. Res. Atmos.* **2020**, *125*, e2019JD030378. [CrossRef]

22. Huai, B.; van den Broeke, M.R.; Reijmer, C.H. Long-term surface energy balance of the western Greenland Ice Sheet and the role of large-scale circulation variability. *Cryosphere* **2020**, *14*, 4181–4199. [CrossRef]

23. Jiang, X.; Wang, N.; He, J.; Wu, X.; Song, G. A distributed surface energy and mass balance model and its application to a mountain glacier in China. *Chin. Sci. Bull.* **2010**, *55*, 1757–1765. [CrossRef]

24. Li, H. Spatial and temporal transferability of Degree-Day Model and Simplified Energy Balance Model: A case study. *Sci. Cold Arid Reg.* **2020**, *12*, 95–103.

25. MacDougall, A.; Wheler, B.; Flowers, G. A preliminary assessment of glacier melt-model parameter sensitivity and transferability in a dry subarctic environment. *Cryosphere* **2011**, *5*, 1011–1028. [CrossRef]

26. Linsbauer, A.; Paul, F.; Machguth, H.; Haeberli, W. Comparing three different methods to model scenarios of future glacier change in the Swiss Alps. *Ann. Glaciol.* **2017**, *54*, 241–253. [CrossRef]

27. Azam, M.F.; Wagnon, P.; Vincent, C.; Ramanathan, A.; Linda, A.; Singh, V.B. Reconstruction of the annual mass balance of Chhota Shigri glacier, Western Himalaya, India, since 1969. *Ann. Glaciol.* **2014**, *55*, 69–80. [CrossRef]

28. Zhang, H.; Li, Z.; Zhou, P.; Zhu, X.; Wang, L.I.N. Mass-balance observations and reconstruction for Haxilegen Glacier No.51, eastern Tien Shan, from 1999 to 2015. *J. Glaciol.* **2018**, *64*, 689–699. [CrossRef]

29. Cazorzi, F.; Dalla Fontana, G. Snowmelt modelling by combining air temperature and a distributed radiation index. *J. Hydrol.* **1996**, *181*, 169–187. [CrossRef]

30. Hock, R. A distributed temperature-index ice-and snowmelt model including potential direct solar radiation. *J. Glaciol.* **1999**, *45*, 101–111. [CrossRef]

31. Pellicciotti, F.; Brock, B.; Strasser, U.; Burlando, P.; Funk, M.; Corripio, J. An enhanced temperature-index glacier melt model including the shortwave radiation balance: Development and testing for Haut Glacier d'Arolla, Switzerland. *J. Glaciol.* **2005**, *51*, 573–587. [CrossRef]

32. Jonsell, U.Y.; Navarro, F.J.; Bañón, M.; Lapazaran, J.J.; Otero, J. Sensitivity of a distributed temperature-radiation index melt model based on AWS observations and surface energy balance fluxes, Hurd Peninsula glaciers, Livingston Island, Antarctica. *Cryosphere* **2012**, *6*, 539–552. [CrossRef]

33. Gabbi, J.; Carenzo, M.; Pellicciotti, F.; Bauder, A.; Funk, M. A comparison of empirical and physically based glacier surface melt models for long-term simulations of glacier response. *J. Glaciol.* **2014**, *60*, 1140–1154. [CrossRef]

34. Du, W.; Qin, X.; Liu, Y.; Wang, X. Variation of the Laohugou Glacier No.12 in the Qilian Mountains. *J. Glaciol. Geocryol.* **2008**, *30*, 373–379.

35. Chen, J.; Qin, X.; Kang, S.; Du, W.; Sun, W.; Liu, Y. Potential Effect of Black Carbon on Glacier Mass Balance during the Past 55 Years of Laohugou Glacier No. 12, Western Qilian Mountains. *J. Earth Sci.* **2020**, *31*, 410–418. [CrossRef]

36. Liu, Y.; Qin, X.; Chen, J.; Li, Z.; Wang, J.; Du, W.; Guo, W. Variations of Laohugou Glacier No. 12 in the western Qilian Mountains, China, from 1957 to 2015. *J. Mt. Sci.* **2018**, *15*, 25–32. [CrossRef]

37. Zou, X.; Sun, W.; Yang, D.; Wang, Y.; Li, Y.; Jin, Z.; Du, W.; Qin, X. Effect of cloud on surface energy balance of Laohugou Glacier No.12, Qilian Mountains. *J. Glaciol. Geocryol.* **2022**, *43*, 342–356.

38. Sun, W.; Qin, X.; Du, W.; Liu, W.; Liu, Y.; Zhang, T.; Xu, Y.; Zhao, Q.; Wu, J.; Ren, J. Ablation modeling and surface energy budget in the ablation zone of Laohugou glacier No. 12, western Qilian mountains, China. *Ann. Glaciol.* **2014**, *55*, 111–120. [CrossRef]

39. Wang, L. Simulation and reconstruction of glaciers mass balance in Qilian Mountains from 1961 to 2013. Ph.D. Thesis, University of Chinese Academy of Sciences, Beijing, China, 2022.

40. Huai, B.; Wang, J.; Sun, W.; Wang, Y.; Zhang, W. Evaluation of the near-surface climate of the recent global atmospheric reanalysis for Qilian Mountains, Qinghai-Tibet Plateau. *Atmos. Res.* **2021**, *250*, 105401. [CrossRef]

41. Wang, Y.; Sun, W.; Wang, L.; Li, Y.; Du, W.; Chen, J.; Qin, X. How do different reanalysis radiation datasets perform in west Qilian Mountains? *Front. Earth Sci.* **2022**, *10*, 241. [CrossRef]

42. Chen, J.; Kang, S.; Qin, X.; Du, W.; Sun, W.; Liu, Y. The mass-balance characteristics and sensitivities to climate variables of Laohugou Glacier No. 12, western Qilian Mountains, China. *Sci. Cold Arid Reg.* **2017**, *9*, 543–553.
43. Jin, Z.; Qin, X.; Sun, W.; Chen, J.; Zhang, X.; Liu, Y.; Li, Y. Monthly variations of temperature gradient in glacierized and non-glacierized areas of the western Qilian Mountains. *J. Glaciol. Geocryol.* **2019**, *41*, 282–292.
44. Huintjes, E.; Sauter, T.; Schroeter, B.; Maussion, F.; Yang, W.; Kropacek, J.; Buchroithner, M.; Scherer, D.; Kang, S.; Schneider, C. Evaluation of a coupled snow and energy balance model for Zhadang glacier, Tibetan Plateau, using glaciological measurements and time-lapse photography. *Arc. Antarct. Alp. Res.* **2015**, *47*, 573–590. [CrossRef]
45. Kang, E.; Cheng, G.; Lan, Y.; Jin, H. A model for simulating the response of runoff from the mountainous watersheds of inland river basins in the arid area of northwest China to climatic changes. *Sci. China Ser. D Earth Sci.* **1999**, *42*, 52–63. [CrossRef]
46. Sun, W.; Qin, X.; Ren, J.; Wu, J.; Du, W.; Liu, Y.; Hou, D. Surface Energy Balance in the Accumulation Zone of the Laohugou Glacier No.12 in the Qilian Mountains during Ablation Period. *J. Glaciol. Geocryol.* **2011**, *33*, 38–46.
47. Oke, T.R. *Boundary Layer Climates*; Routledge: London, UK, 2002.
48. Hock, R. Glacier melt: A review of processes and their modelling. *Prog. Phys. Geogr. Earth Environ.* **2005**, *29*, 362–391. [CrossRef]
49. Brock, B.W.; Willis, I.C.; Sharp, M.J. Measurement and parameterization of albedo variations at Haut Glacier d'Arolla, Switzerland. *J. Glaciol.* **2000**, *46*, 675–688. [CrossRef]
50. Jiang, X.; Wang, N.; He, J.; Song, G.; Yang, S.; Wu, X. A Study of Parameterization of Albedo on the Qiyi Glacier in Qilian Mountains, China. *J. Glaciol. Geocryol.* **2011**, *33*, 30–37.
51. Gao, L.; Hao, L.; Chen, X. Evaluation of ERA-interim monthly temperature data over the Tibetan Plateau. *J. Mt. Sci.* **2014**, *11*, 1154–1168. [CrossRef]
52. Zhao, D.; Gao, X.; Wu, S.; Zheng, D. Trend of Climate Variation in China from 1960 to 2018 Based on Natural Regionalization. *Adv. Earth Sc.* **2020**, *35*, 750–760.
53. Liu, Y.; Qin, D.; Li, Y.; Qin, X.; Li, Z.; Wang, J.; Jin, Z.; Wang, L. Changes in the Surface Elevation of the Laohugou Glacier No. 12 in Western Qilian Mountains. *Front. Earth Sci.* **2022**, *10*, 832701. [CrossRef]
54. Ohmura, A. Changes in mountain glaciers and ice caps during the 20th century. *Ann. Glaciol.* **2017**, *43*, 361–368. [CrossRef]
55. Yang, W.; Yao, T.; Guo, X.; Zhu, M.; Li, S.; Kattel, D.B. Mass balance of a maritime glacier on the southeast Tibetan Plateau and its climatic sensitivity. *J. Geophys. Res. Atmos.* **2013**, *118*, 9579–9594. [CrossRef]
56. Wang, S.; Pu, J.; Wang, N. Study of Mass Balance And Sensibility to Climate Change of Qiyi Glacier in Qilian Mountains. *J. Glaciol. Geocryol.* **2011**, *33*, 1214–1221.